Multifunctional Molecularly Imprinted Nanozymes with Improved Enrichment and Specificity for Organic and Inorganic Trace Compounds

Zhanyi Ge, Yilin Zhao*, Jiayi Li, Zhaobo Si Wenbo Du, Haijia Su*

E-mail: suhj@mail.buct.edu.cn; zhaoyl@mail.buct.edu.cn

Supporting information

Materials

Fe_3O_4 NPs(200 nm, Beijing GiGNano Biointerface Company), tetraethyl orthosilicate (TEOS, AR grade, Sigma-Aldrich), hydrogen peroxide (30% w/v, Macklin), Argon gas (AR grade, Beijing Chemical Works), methanol (CP grade, Macklin), ethylene dimethacrylate (EGDMA, AR grade, Macklin), azodiisobutyronitrile (AIBN, AR grade, Macklin), $Pb(NO_3)_2$(AR grade, Xilong Chemical Co.,ltd.), 2-(2-aminophenyl) benzimidazole (AR grade, Aladdin), 4-vinyl pyridine (4-VP, AR grade, Aladdin), methacrylic acid (MAA, AR grade, Macklin), acetonitrile (AR grade, Macklin), ethylene diamine tetraacetic acid(EDTA, AR grade, Fuchen Chemical Reagent Co., Ltd.), glacial acetic acid (AR grade, Beijing Chemical Works), sodium acetate (AR grade, Fuchen Chemical Reagent Co., Ltd.), 2,2′-azino-bis(3-ethylbenzothiazoline- 6-sulfonic acid) (ABTS, AR grade, Sigma-Aldrich), ethanol (98% w/v, Beijing Chemical Works), ammonia solution (25% w/v, Fuchen Chemical Reagent Co., Ltd.), imidazole (AR grade, Aladdin), dimethylimidazole (DMI, AR grade, Aladdin), triallyl cyanurate (TAT, AR grade, Aladdin), 4-phenoxyphenylacetonitrile (4-PPACN, AR grade, Aladdin), dibutyl phthalate (DBP, AR grade, Aladdin), diazinon (DIZ, AR grade, Aladdin), hydrofluoric acid (40% w/v, Macklin), sodium hydroxide (AR grade, Macklin)

Characterization

Scanning electron microscope (SEM). SEM images of the prepared nanoparticles were collected on a scanning electron microscope (ZEISS GeminiSEM 300, GRE), with the samples fixed with conductive adhesive and then sprayed with gold.

Transmission electron microscope (TEM). Nanoparticles were examined by TEM (FEI Tecnai F20, USA) using a copper mesh to prepare the samples and ethanol as dispersant, as well as energy dispersive spectroscopy (EDS).

X-Ray Diffraction (XRD). XRD patterns of the prepared NPs were obtained using the Ultima IV x-ray diffractometer (Rigaku, Japan).

Thermogravimetric Analysis (TGA). TG data were obtained by heating from room temperature to 5500°C at 20°C/min using a thermo gravimetric analyser (SDT Q600, TA Instruments, USA) under a dynamic N_2 atmosphere.

Fourier transform infrared spectroscopy (FT-IR). A Fourier transform infrared spectrometer Nicolet 6700 (Thermo Fisher, America) was used to analyze the FT-IR spectrum of Fe_3O_4 NPs and IIP@void@Fe_3O_4 nanozymes.

Vibrating sample magnetometers (VSM, Lakeshore 7407, USA) were applied to measure magnetization curves of samples at 2 T magnetic field strength.

X-ray photoelectron spectroscopy (XPS). An ESCA PHI500 X-ray photoelectron spectroscopy apparatus was used to measure the spectra of the adsorbent with and

without the target pollutants.

^1H NMR spectra was used to analyse the interactions between the Target substrate and the imprinting sites by chemical shifts of the associated protons. 1H NMR spectra of the imprinted polymers were obtained using a Bruker Avance 600 spectrometer (Bruker Co., Germany). In this context, 4 mM of DIZ, 47 mM of MAA and the mixture containing 4 mM of DIZ and 47 mM of MAA and 0.4 M of EGDMA and 12 mM of AIBN were dissolved in DMSO, respectively.

The preparation process of the IIP@void@Fe_3O_4

The preparation process of the IIP@void@Fe_3O_4 for enrichment and determination of Pb^{2+} was similar to that of MIP@void@Fe_3O_4. The difference is that, in step III, an ion imprinted polymer shell is coated on the surface of the modified SiO_2@Fe_3O_4NPs. Briefly, Pb $(NO_3)_2$ (0.0166 g), 2-(2-Aminophenyl) benzimidazole (Benzenamine) (0.0105 g) and 4-vinyl pyridine (4-vp, 20 μL) were dissolved by 50 mL acetonitrile. The mixture solution was pre-combine for 5 h under stirring. Then SiO_2@Fe_3O_4NPs (0.06 g), EGDMA (1.5 mL) and AIBN (0.08g) were added into the solution. The solution was completely and evenly dispersed under ultrasonic irradiation, followed by stirring at 65 ℃ under Ar_2 for 24 h. The unpolymerized monomers and unimprinted templates were removed by washed and magnetically collected. To elute templates in the imprinted shell, the Fe_3O_4@SiO_2@MIP were eluated in 50 mL methanol with 0.01 M EDTA and 0.1 M HCl under stirring for 12 h,

and the obtained nanozyme were collected magnetically washed after and dried at 60 °C for 3 h. After etched to form the yolk-shell structure, the formed IIP@void@Fe_3O_4 nanozymes were collected magnetically washed after and dried at 60 °C for 3 h.

Adsorption experiment of Pb^{2+}

The adsorption of Pb^{2+} was studied by batch experiments, each of which was repeated three times. In the static adsorption experiment, IIP@void@Fe_3O_4 nanozymes of the same quality were dispersed in different concentrations of Pb^{2+} solutions. The solutions were shaken at 300 rpm at 37 ℃ for a certain time until adsorption equilibrium. After centrifugation, the concentrations of Pb^{2+} were determined by ICP-MC. In the adsorption kinetics experiments, identical masses of IIP@void@Fe_3O_4 nanozymes were dispersed in Pb^{2+} solutions of uniform concentration. The experiments were conducted at 37°C with continuous shaking at 300 rpm for varying durations, after which the residual Pb^{2+} concentration was measured. The adsorption capacity of Pb^{2+} is expressed as adsorption quality (Q), which can be calculated as follows:

$$Q = \frac{(C_0 - Ce) \times V}{M}$$

where Q (mg/g) is the equilibrium adsorption quality of IIP@void@Fe_3O_4 on Pb^{2+}, and C_0 (mg/L) and Ce (mg/L) are initial and final concentration of Pb^{2+} in the solution, respectively. V (mL) refers to the volume of the sample and M (g) is the weight of IIP@void@Fe_3O_4.

The detection method of Pb^{2+}

Gradient concentrations of Pb^{2+} were assayed as follows: Pb^{2+} was added into Hac/NaAc buffer solution (final concentration of 200 mM) to establish experimental groups of different concentrations. IIP@void@Fe_3O_4 was introduced into these solutions and shaken for a period of time. After incubation, ABTS solution (final concentration 0.1 mM) and H_2O_2 solution (final concentration 0.4 mM) were added to the mixture. The experiments were performed in the dark for a set period. The absorbance of the solutions was characterized using a TECAN Infinite M200 Pro multi-function microplate reader. The absorbance of the blank group without Pb^{2+} was recorded as A_0, and the difference between A_0 and the absorbance (A) measured in the experiment was closely related to the concentration of Pb^{2+}. For specific detection, IIP@void@Fe_3O_4 was introduced into a solution of Pb^{2+} and other metal ions at the same concentration, and the mixture was shaken for a period of time. After incubation, ABTS solution (final concentration 0.1 mM) and H_2O_2 solution (final concentration 0.4 mM) were added. After the same detection method, the difference of absorbance (A) measured in metal ions detection experiment and A_0 reflects the selectivity of the detection method

Quantitative detection by smart detection app

The solutions in section 2.3 were used for the smart detection app modules to quantitatively detect the concentration of Pb^{+} and DIZ based on RGB color mode. Specifically, reaction mixtures with different concentrations of Pb^{2+} (1×10^{-8}, 1×10^{-7}, 1×10^{-6}, 1×10^{-5}, 1×10^{-4}, 1×10^{-3}, $1\times1^{0-2}$ ppm) and DIZ solution (1×10^{-4}, 1×10^{-5}, 1×10^{-6},

1×10^{-7}, 1×10^{-8}, 1×10^{-9}, 1×10^{-11} M) were collected in colorimetric dishes and captured using the developed app. Then, based on the RGB color mode analysis was performed on the obtained brightness values and R, G, B, G/B (green brightness divided by blue brightness), R/B (red brightness divided by blue brightness), and G/R (green brightness divided by red brightness) were intelligently calculated. Finally, the corresponding detection standard curve was established and used for the detection of actual samples.

The detection method of actual samples

To assess the presence of Pb^{2+} in actual samples, a specified concentration of Pb^{2+} standard solution was added to both Industrial wastewater and Kitchen wastewater. The mixture was then incubated with MIPI nanozymes for 2 hours. Following the incubation period, ABTS and hydrogen peroxide solutions were introduced, and the resulting reaction mixture was left to incubate in darkness for 30 minutes, after which absorbance readings were recorded. The absorbance values were utilized in a linear detection equation to evaluate the disparities between the detected concentrations and the actual concentrations of Pb^{2+}. The Recovery and RSDS (Relative Standard Deviation of the Signal) were subsequently calculated to assess the accuracy and precision of the detection method. This methodology aimed to provide insights into the presence and quantification of Pb^{2+} in industrial and kitchen wastewater samples.

Regeneration and reusability study of Pb^{2+}

149 Five cycles of adsorption-elution experiments were performed on IIP@void@Fe_3O_4.
150 In each cycle, 2.5 mg of IIP@void@Fe_3O_4 nanozyme was introduced into 5 mL of
151 Pb^{2+} solution (5 ppm) and incubated for 2 h. Pb^{2+} in supernatant concentrations were
152 determined by ICP-MC after magnetic recovery. These IIP@void@Fe_3O_4 nanozymes
153 were regenerated after washing and drying before the next cycle of the adsorption
154 experiment.

155

Results and discussion

Characterization of IIP@void@Fe_3O_4 nanozyme

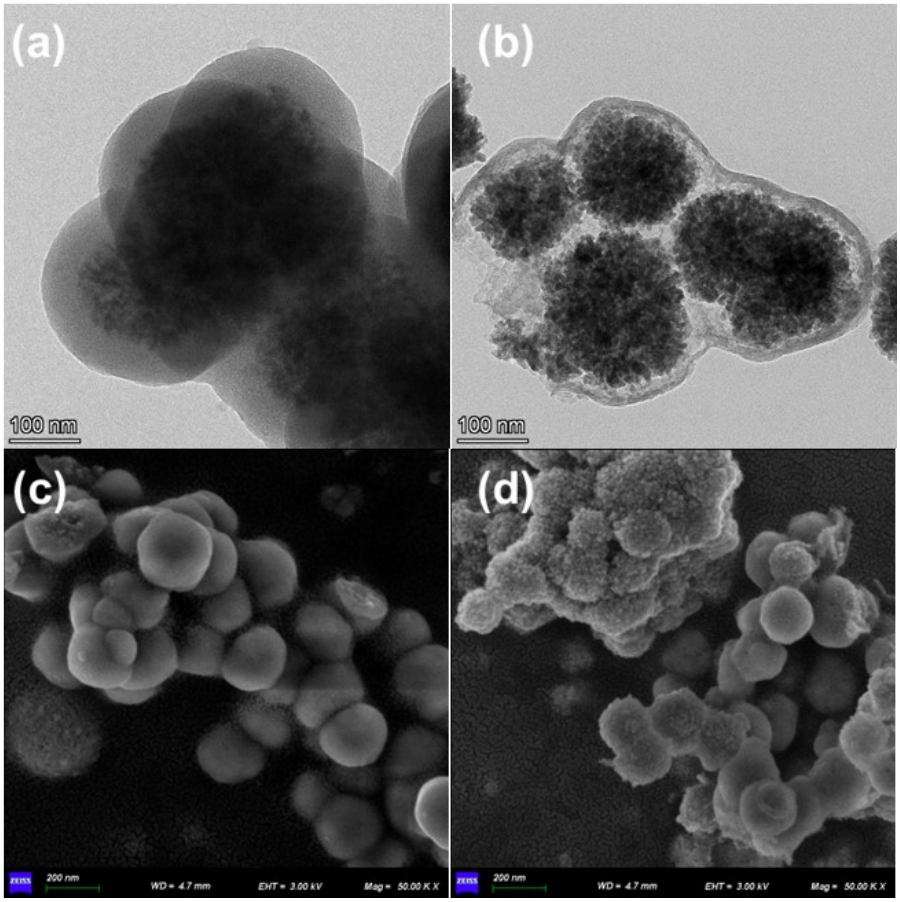

Fig.S1 TEM images of (a) NIP@SiO_2@Fe_3O_4 and (b) IIP@void@Fe_3O_4 nanozyme. SEM images of (c) NIP@SiO_2@Fe_3O_4 and (d) IIP@void@Fe_3O_4 nanozyme.

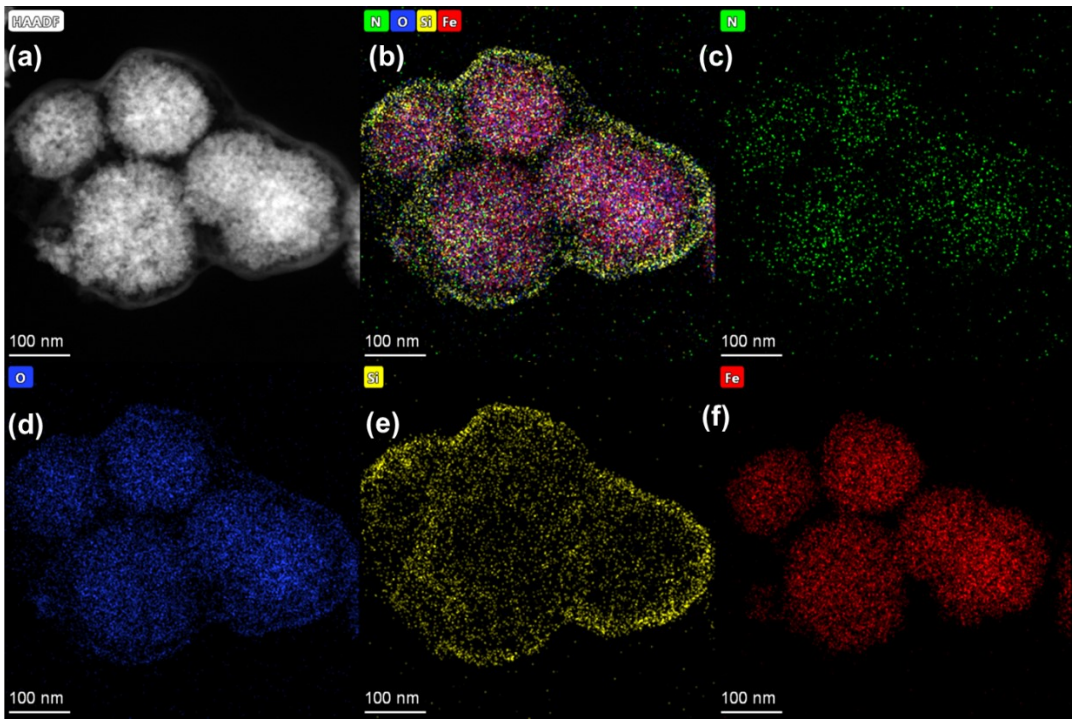

Fig. S2 EDX chemical mapping of IIP@void@Fe_3O_4 nanozyme. (a) HAADF-STEM image of the area studied; (b) Superimposition of iron (red), oxygen (blue), silicon (yellow) and nitrogen (green) distribution. Distribution of nitrogen (c); the distribution of oxygen (d); the distribution of silicon (e); and the distribution of iron (f), respectively.

Upon comparing Figures S1a and S1b, it is evident that the IIP@void@Fe_3O_4 nanozyme exhibits a distinct hollow structure following the etching of the SiO_2 shell. This observation is further corroborated by SEM images. In Figure S1c, the NIP@SiO_2@Fe_3O_4 appears as a full-bodied sphere. However, Figure S1d reveals that the IIP@void@Fe_3O_4 spheres are not only reduced in size but also exhibit partial collapse. This collapse is attributed to the loss of support from the imprinted shell during the SiO_2 shell etching process. The elemental distribution

maps presented in Figure S2 confirm the successful synthesis of the core-shell hollow structure in IIP@void@Fe_3O_4 nanozyme. A clear demarcation between silicon and iron elements is observed (Figure S2b), further validating the the hollow layer of the intended nanozyme.

Adsorption properties of MIP@void@Fe_3O_4

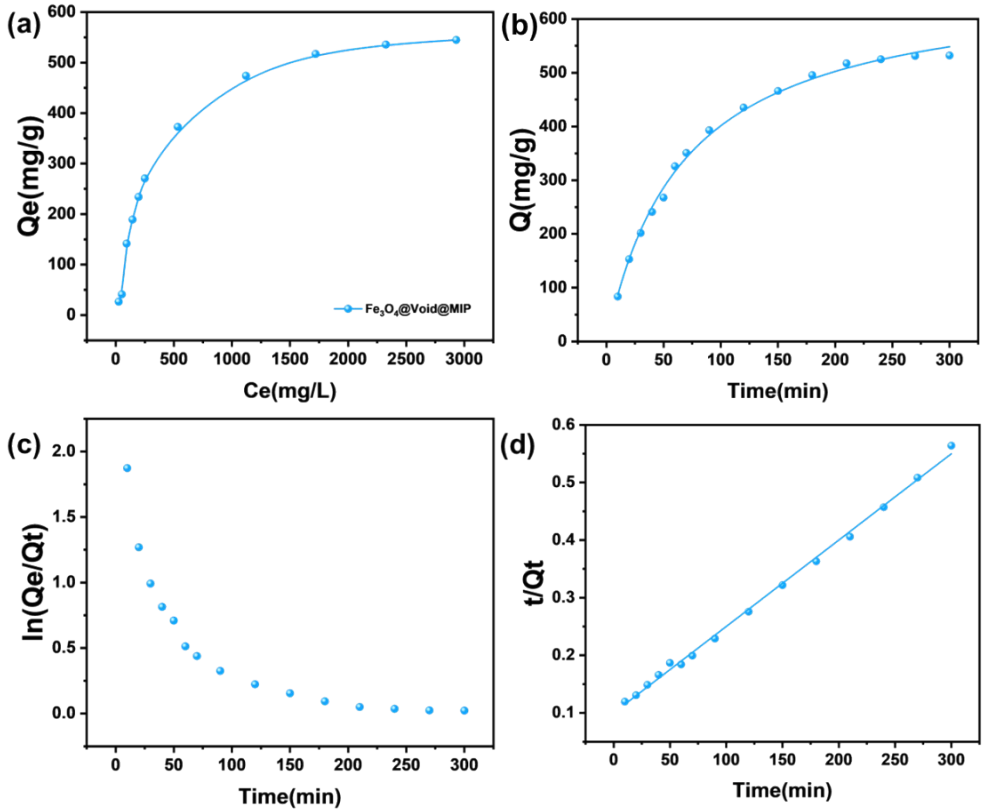

Fig. S3 (a) Adsorption isotherm of DIZ by MIP@void@Fe_3O_4; (b) adsorption kinetic curves of DIZ by MIP@void@Fe_3O_4; (c) linear plot of Pseudo-first-order model; (d) linear plot of Pseudo-second-order model;

The adsorption isotherm, as depicted in Figure S3, furnishes pivotal insights into the selective adsorption process of DIZ by MIP@void@Fe_3O_4. In Fig. S3a, the adsorption of MIP@void@Fe_3O_4 exhibited a rapid increase with escalating initial concentrations, reaching saturation at concentrations exceeding 3040 mg/L, in accordance with the Langmuir model. Furthermore, Figure S3b illustrated that the adsorption of MIP@void@Fe_3O_4 increased sharply with time, attaining its maximum value after 240 minutes, in accordance with a pseudo-second-order kinetic model. Figures S3c and S3d present linear curves based on the first-order and pseudo-second-

192 order kinetic models, respectively. The experimental results indicate a clear
193 conformity of the adsorption kinetics with the pseudo-second-order kinetic model.
194 The results indicated that the adsorption capacity of MIP@void@Fe_3O_4 was
195 influenced by the electron sharing or transfer between adsorbent and adsorbent, and
196 was mainly affected by chemical adsorption mechanism.
197

Effect of buffer solution on catalytic oxidation

The colorimetric ability of Fe_3O_4 nanozymes was investigated in different kinds of buffer solutions with pH values of 4, and the results are shown in Fig. S1. It was found that the absorbance of the Hac/NaAc buffer solution at 420 nm was significantly higher than that of the phosphoric acid buffer solution (PB) and citric acid/sodium citrate buffer solution at 420 nm. This phenomenon indicated that Fe_3O_4 nanozymes showed obvious catalytic capacity in Hac/NaAc buffer solution, but had weak catalytic capacity in phosphate buffer solution and citric acid/sodium citrate buffer solution. Therefore, subsequent experiments were conducted in Hac/NaAc buffer solution.

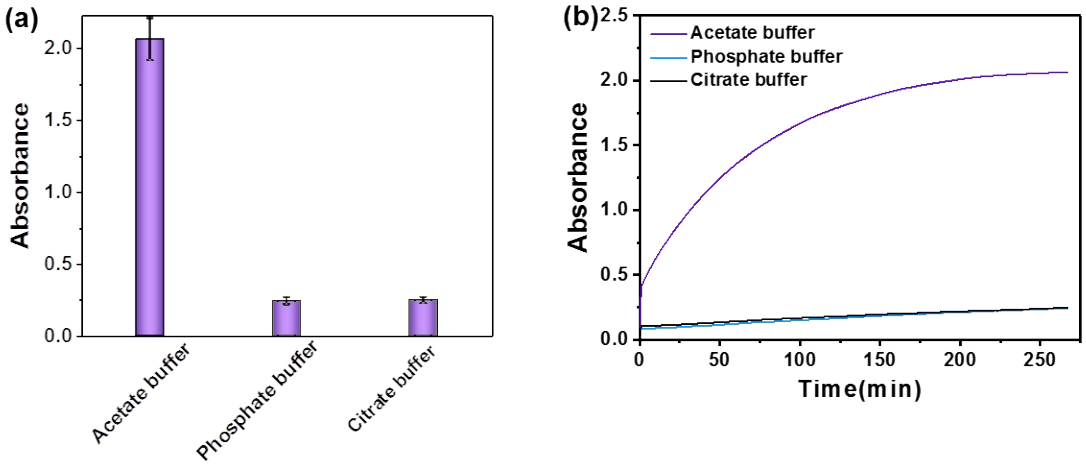

Fig S4. (a) Absorbance at 420 nm of ABTS oxidized by H_2O_2 catalyzed by Fe_3O_4 nanozymes in different buffer solution environments after 180 min. The final concentration of these buffers was 200 mM. (b) Time-dependent concentration of oxABTS determined for oxidization catalyzed by Fe_3O_4 nanozymes at 25 °C. The concentration of ABTS, H_2O_2 and Fe_3O_4 nanozymes were 10 mM, 40 mM, and 20mg/mL respectively.

Sensing properties of multifunctional core-shell mesoporous microspheres

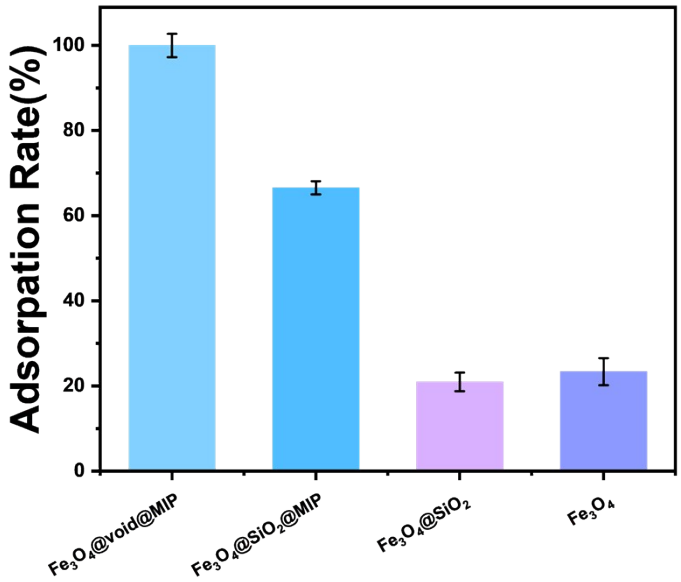

Fig S5 The adsorption ratio of different particles to DIZ

Figure S5 illustrates the adsorption ratios of DIZ by Fe_3O_4, Fe_3O_4@SiO_2, Fe_3O_4@SiO_2@MIP, and MIP@void@Fe_3O_4. Interestingly, the trend indicates that MIP@void@Fe_3O_4 exhibits a higher adsorption capacity compared to Fe_3O_4@SiO_2@MIP, Fe_3O_4, and Fe_3O_4@SiO_2. This suggests that Fe_3O_4 itself doesn't possess a strong adsorption capacity for DIZ. Moreover, the adsorption capacity appears to decrease after the encapsulation of SiO_2 due to hindered mass transfer. However, upon the addition of a molecularly imprinted polymer shell, the adsorption capability notably increases. Additionally, after etching off the SiO_2 shell, the adsorption capacity further improves. This highlights the efficient adsorption ability of the molecularly imprinted nanozyme with a core-shell hollow structure for DIZ. Furthermore, the hollow structure enhances mass transfer, providing more binding sites for DIZ, consequently enhancing the adsorption ratio.

XPS survey

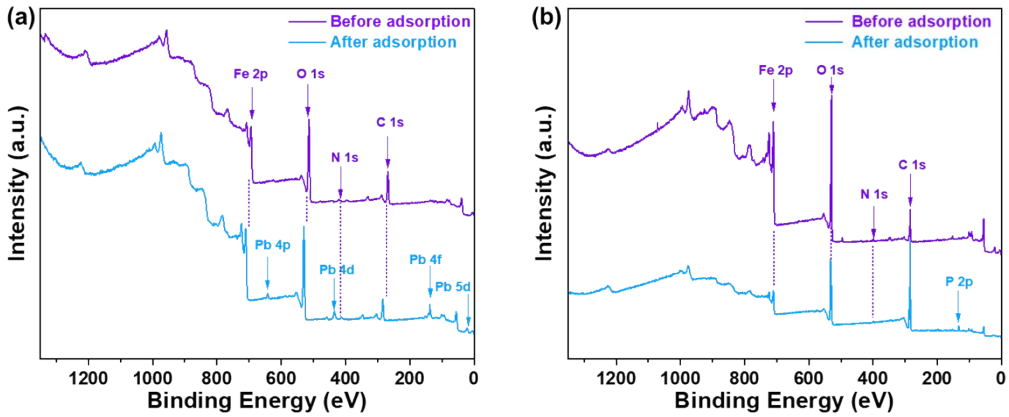

Fig S6 (a) XPS survey of IIP@void@Fe_3O_4 before and after Pb^{2+} adsorption, (b) XPS survey of MIP@void@Fe_3O_4 before and after DIZ adsorption

Figure S6(a) in the XPS spectrum clearly exhibits characteristic peaks of Pb 4p, Pb 4d, Pb 4f, and Pb 5d, indicating the successful adsorption of Pb by MIP@void@Fe_3O_4. Similarly, Figure S6(b) shows the appearance of a characteristic peak of P 2p in the XPS spectrum after the adsorption of DIZ by MIP@void@Fe_3O_4. Considering that only DIZ in our sample contains phosphorus (P), this confirms the successful adsorption of DIZ by our molecularly imprinted nanozyme.

Michaelis-Menten plot for H_2O_2 oxidation by MIP@void@Fe_3O_4, NIP@void@Fe_3O_4, SiO_2@$Fe_3O_4$and Fe_3O_4

The comparative analysis of peroxidase-like activity among different nanozymes, as illustrated in Fig S7 and Table S1, reveals that the amino-modified Fe_3O_4 nanozymes exhibit the highest peroxidase activity. The encapsulation with a silica (SiO_2) shell notably inhibits both the peroxidase activity and substrate affinity of these nanozymes. However, a significant enhancement in peroxidase activity is observed upon etching away the SiO_2 shell, bringing the activity level on par with that of the original Fe_3O_4 nanozymes. This enhancement aligns with the design rationale of our study; removing the SiO_2 shell substantially improves the mass transfer efficiency of hydrogen peroxide, thereby augmenting the catalytic peroxidase activity of the nanozymes. This finding underscores the efficacy of our structural design in optimizing enzymatic function.

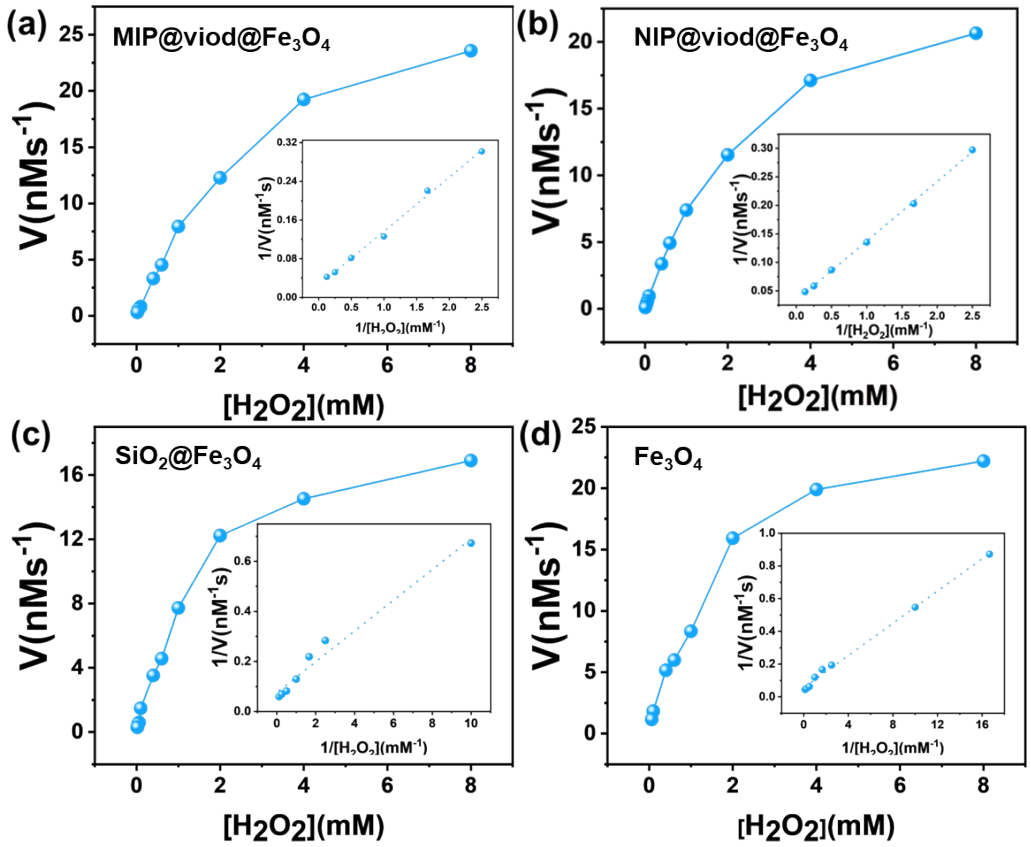

Fig S7 Michaelis-Menten plot for H_2O_2 oxidation by MIP@void@Fe_3O_4(a), NIP@void@Fe_3O_4(b), SiO_2@Fe_3O_4(c)and Fe_3O_4(d)

Table S1. Comparison of *Km* and *Vmax* for IIP@void@Fe_3O_4, MIP@void@Fe_3O_4, NIP@void@Fe_3O_4, SiO_2@Fe_3O_4 and Fe_3O_4 NPs

Sample	*Vmax* (10^{-9}M/s)	*Km*(mM)	Ref.
HRP	0.689	10.35	[1]
Fe_3O_4	33.14	2.75	Our work
Fe_3O_4@SiO_2	25.813	2.84	Our work
NIP@void@Fe_3O_4	30.28	3.16	Our work
IIP@void@Fe_3O_4	30.02	3.01	Our work
MIP@void@Fe_3O_4	33.26	3.22	Our work

Comparison of actual sample test parameters

Table S2. Selective detection methods of Pb^{2+} and pesticide in environmental samples

Substance	Detection Method	LOD	Testing sample	Ref.
Pb	HR-CS FAAS	0.24 μg L^{-1}	Water, cola and fruit juice	[2]
Pb	Electrochemical biosensors	4.76 μg L^{-1}	Water	[3]
Pb	DNA-Catalyzed Porphyrin Metalation	4.75 μg L^{-1}	Water	[4]
Pb	Ion-imprinted fluorescence probe	5.25 μg L^{-1}	Water	[5]
Pb	Bionic ion imprinted nanozyme	0.0097 μg L^{-1}	Water	Our work
Glyphosate	HPLC-MS	0.25 μg/L	Water	[6]
Terbufos	FPSE/GC-MS	0.033 μg/L	Agricultural products	[7]
Glyphosate	Immunosensor fluorescence magnetic nanoparticles	0.055 μg L^{-1}	Agricultural products	[8]
Malathion	AChE-CS/3DG-CuO NFs	310 μg L^{-1}	Water	[9]
Parathion	Origami paper-based electrochemical biosensor	2 μgL^{-1}	Water	[10]
DIZ	FL-AChE-ATCh-UCNPs-Cu	0.05 μg/L^{-1}	Water	[11]
DIZ	Bionic molecular imprinted nanozyme	0.030 μgL^{-1}	Water	Our work

Reference

[1] K. Fan, H. Wang, J. Xi, Q. Liu, X. Meng, D. Duan, L. Gao, X. Yan, Optimization of Fe3O4 nanozyme activity via single amino acid modification mimicking an enzyme active site, Chemical Communications, 53 (2016).
[2] H. Ciftci, C. Er, O. Yalcinkaya, M.M. Temuz, A.R. Turker, High-resolution continuum source flame atomic absorption spectrometric (HR-CS FAAS) determination of trace aluminium and lead in water and some beverage samples after separation and preconcentration procedure, International Journal of Environmental Analytical Chemistry, 94 (2014) 579-593.
[3] J. Guo, H. Huang, M. Zhou, C. Yang, L. Kong, Quantum Dots-Doped Tapered Hydrogel Waveguide for Ratiometric Sensing of Metal Ions, Anal Chem, 90 (2018) 12292-12298.
[4] D. Peng, Y. Li, Z. Huang, R.-P. Liang, J.-D. Qiu, J. Liu, Efficient DNA-Catalyzed Porphyrin Metalation for Fluorescent Ratiometric Pb2+ Detection, Analytical Chemistry, 91 (2019) 11403-11408.
[5] H. Lu, C. Yu, S. Xu, A dual reference ion-imprinted ratiometric fluorescence probe for simultaneous detection of silver (I) and lead (II), Sensors and Actuators B: Chemical, 288 (2019) 691-698.
[6] Elena, Okada, Timothy, Coggan, Tarun, Anumol, Bradley, Clarke, Graeme, Allinson, A simple and rapid direct injection method for the determination of glyphosate and AMPA in environmental water samples, ANALYTICAL AND BIOANALYTICAL CHEMISTRY, (2018).
[7] R. Kaur, R. Kaur, S. Rani, A.K. Malik, A. Kabir, K.G. Furton, Application of fabric phase sorptive extraction with gas chromatography and mass spectrometry for the determination of organophosphorus pesticides in selected vegetable samples, Journal of Separation Science, 42 (2019).
[8] H.U. Lee, D.U. Jung, J.H. Lee, Y.S. Song, C. Park, S.W. Kim, Detection of glyphosate by quantitative analysis of fluorescence and single DNA using DNA-labeled fluorescent magnetic core–shell nanoparticles, Sensors & Actuators B Chemical, 177 (2013) 879-886.
[9] J. Bao, T. Huang, Z. Wang, H. Yang, C. Hou, 3D Graphene/Copper Oxide Nano-flowers Based Acetylcholinesterase Biosensor for Sensitive Detection of Organophosphate Pesticides, Sensors and Actuators B Chemical, 279 (2018).
[10] Arduini, Cinti, Caratelli, Amendola, Palleschi, Moscone, Origami multiple paper-based electrochemical biosensors for pesticide detection, Biosensors & Bioelectronics, (2018).
[11] P. Wang, H. Li, M.M. Hassan, Z. Guo, Z.Z. Zhang, Q. Chen, Fabricating an Acetylcholinesterase Modulated UCNPs-Cu 2+ Fluorescence Biosensor for Ultrasensitive Detection of Organophosphorus Pesticides-Diazinon in Food, Journal of Agricultural and Food Chemistry, (2019).